Ultra-fast and high-stable near-pseudocapacitance intercalation cathode for aqueous potassium-ion storage

Meng Huang [a], Xuanpeng Wang [b,c,**], Jiashen Meng [a], Xiong Liu [a], Xuhui Yao [d], Ziang Liu [a], Liqiang Mai [a,c,*]

[a] State Key Laboratory of Advanced Technology for Materials Synthesis and Processing, School of Materials Science and Engineering, Wuhan University of Technology, Wuhan, 430070, PR China
[b] Department of Physical Science & Technology, School of Science, Wuhan University of Technology, Wuhan, 430070, PR China
[c] Foshan Xianhu Laboratory of the Advanced Energy Science and Technology Guangdong Laboratory, Xianhu hydrogen Valley, Foshan 528200, China
[d] Advanced Technology Institute, University of Surrey, Guildford, Surrey, GU2 7XH, United Kingdom

ABSTRACT

The intrinsically limited rate capability of batteries by the diffusion-controlled ionic storage mechanism is still existing, and long-service batteries are always required for low-cost grid-scale energy storage. Herein, we design and construct a series of Ni_xZn_yHCF (x + y = 3, x = 1, 1.5 or 2) bimetallic Prussian blue analogues as cathode materials for aqueous potassium-ion batteries. On the basis of electrochemical and structural analysis, a synergistic effect between stable Ni^{2+} and high-voltage Zn^{2+} in Ni_2Zn_1HCF is demonstrated, which simultaneously promises ultrafast near-pseudocapacitance intercalation and super-stable potassium storage. As presented, Ni_2Zn_1HCF cathode shows an extraordinary high-rate capability of 1000C with a capacity retention of 66% and a high capacity recovery of 95.3%, which derives from the large sufeace area and fast near-pseudocapacitive intercalation mechanism. When cycled at 1000C for 80,000 times, a negligible capacity decay of 0.000385% per cycle further proves this cathode to be high-rate and ultra-stable. In addition, the highly reversible solid-solution K^+ intercalation/extraction mechanism in the Ni_2Zn_1HCF cathode is illustrated by the *in-situ* X-ray diffraction. This work presents a promising cathode for building ultrafast and long-service aqueous potassium-ion batteries.

1. Introduction

In recent years, the increasing consumption of fossil fuel contributes to the continuous and extensive emissions of greenhouse gases, thus leading to severe global warming [1]. For sustaining social and technological developments, various sustainable energy resources have been exploited, such as solar, wind and hydroelectric power, and so on [2]. Electrical energy storage has been developed to enable a transition to "green energy", which plays a significant role in storing and transporting these energies [3,4]. Rechargeable batteries as high-efficiency electrochemical energy storage systems are considered as one of the most promising techniques to bridge the connection between the power grid and consumers [5]. Thus, efficient and low-cost grid-scale rechargeable batteries are highly desired, while environmental friendly and health

harmless are also important indicators [6]. Among these rechargeable battery systems, the commercial lithium-ion batteries (LIBs), showing long service life, high energy and efficiency after decades of development, have occupied the most share of the portable market, including cellphones and laptops [7]. However, high costs because of the critical manufacturing processes and the scarcity of lithium and cobalt resources, as well as flammable and poisonous organic electrolytes make them not suitable in grid-scale energy storage and intermittent power supply [8]. Non-aqueous sodium-ion batteries (SIBs) and potassium-ion batteries (PIBs) have received much attention since the 21st century because of their abundant and available resources [9–11]. Whereas, they exhibit the same issues as LIBs do in addition to the unstable nature of sodium and potassium metals, so non-aqueous SIBs and PIBs also have no superiority in high-safety and low-cost energy storage.

Nowadays, aqueous rechargeable alkali-metal ion (Li^+, Na^+ and K^+) batteries (ARABs) have shown great potential in grid-scale energy storage and intermittent power supply for their low cost, high safety and fast ionic diffusion [8,12,13]. The usage of aqueous electrolytes instead of organic ones has simplified the manufacturing conditions and largely lowered the flammability [14]. The first establishment of aqueous rechargeable LIBs with $VO_2(B)$ anode and $LiMn_2O_4$ cathode in 1994 marked the beginning of the ARABs' research and development [15]. The analogue aqueous rechargeable SIBs have also received serious attention for the abundance of sodium resources [16]. In the past decades, aqueous rechargeable LIBs and SIBs have experienced rapid progress for stationary application [8]. Among all the ARABs, many researchers have reported that aqueous rechargeable PIBs possess the most superiority on two aspects: K^+ has highest standard intercalation/extraction potential; the smallest Stokes radius of solvated K^+ enables much faster ionic conducting for K^+-based aqueous electrolytes [17–21].

However, it is well known that the energy/power density of ARABs has been greatly limited due to the electrolysis of H_2O above 1.23 V [22]. Although, "water-in-salt" [23], "water-in-bisalt" [24] and hydrate-melt electrolytes [25] have broken the electrochemical stability limitation of 1.23 V, low-cost salts are needed to promote the commercialization of these superconcentrated electrolytes. To better meet the requirements of low-cost and ultra-fast energy storage device for grid-scale energy storage and intermittent power supply, long service life will surely lower the cost per kilowatt-hour, and high-rate will ensure the fast-changing output fluctuations in the grid [26]. In recent years, Prussian blue analogues (PBAs) cathode materials, with typical open-framework structure, have been vastly studied for grid-scale ARABs [20,21,27,28]. Su et al. reported a $K_2Fe^{II}[Fe^{II}(CN)_6]•2H_2O$ nanocubes cathode material which exhibited a high discharge capacity of 120 mAh g^{-1} at 1.4C, while a capacity retention of >85% after a short cycling life of 500 times at 21.4C. This short service-life and low-rate performance could be assigned to the large volume variation during the two-electron reaction processes [29]. A potassium-rich mesoporous $K_2NiFe(CN)_6•1.2H_2O$ cathode, showing high-rate capability and long-service life because of the large channel size and small volume variation during K^+ insertion/extraction, was reported by Ren et al. [30]. This cathode showed an ultrafast charge/discharge rate at 500C, which was completed within 4.1 s, and a lifespan of 5000 times cycling with a high capacity retention of 98.6%. In Huang's recent paper, a zinc hexacyanoferrate cathode also showed excellent rate performances of 300C with capacity retention of 60%, but poor cycling performance due to the dissolution problem of the active materials [31]. Until now, the rate ability of the batteries is intrinsically hindered by the diffusion-controlled ionic storage mechanism. However, faradaic surface redox reactions are promising for high-rate capability [32]; and endless pursuit for long-service energy storage systems is still an effective way to lower the cost per kilowatt-hour, especially for the aqueous batteries [33].

Herein, a series of ultrafast and stable bimetallic Ni_xZn_yHCF ($x + y = 3$, $x = 1$, 1.5 or 2) cathodes for aqueous rechargeable PIBs are reported. The representative Ni_2Zn_1HCF cathode with near-pseudocapacitance characteristics shows an extremely high-rate capability of 1000C with a capacity retention of 66%. When cycled at 500C for 30,000 times, the cathode exhibits a high capacity retainment of 90%, and it shows a very small capacity decay of 0.000385% per cycle in the 80,000 times long-term cycling at 1000C. Besides, the K^+ solid-solution intercalation/extraction storage mechanism of the Ni_2Zn_1HCF cathode is revealed by advanced in-situ X-ray diffraction (XRD) characterization technique. The relationship of the peak current and the scan rate indicates that the K^+ diffusion is near-pseudocapacitive, which enable the excellent rate capability of the Ni_2Zn_1HCF cathode. The high Ni-content stabilization effect for the superstability of the Ni_2Zn_1HCF cathode is also illustrated.

2. Material and methods

2.1. Material synthesis

The typical synthesis process of Ni_0Zn_3HCF is described as follows: Add 100 mL solution containing 0.05 M $ZnSO_4•7H_2O$ into 100 mL solution dissolving 0.025 M $K_3Fe(CN)_6•H_2O$ drop by drop under stirring at 60 °C for 2 h. After complete reaction, the obtained solution was aged for several hours until the precipitates were collected by centrifugation and washed with water and pure ethanol for 3 times, respectively. The washed solid products were dried at 70 °C for over 12 h. The synthesis process of Ni_3Zn_0HCF is in the same procedure except that the $ZnSO_4•7H_2O$ is changed to $Ni(CHCOO)_2•7H_2O$. The synthesis processes of Ni_2Zn_1HCF, $Ni_{1.5}Zn_{1.5}HCF$ and Ni_1Zn_2HCF are varies in the ratio of Ni $(CHCOO)_2•7H_2O$ to $ZnSO_4•7H_2O$ from 2:1 to 1:1 and 1:2.

2.2. Material characterization

The morphology was observed by using the field emission scanning electron microscopy (SEM, JEOL JSM-7100F, acceleration voltage: 15 kV). Transmission electron microscope (TEM), high-resolution TEM (HRTEM) images and High Angle Annular Dark Field (HAADF) images were collected by using a Titan G2 60–300 with image corrector. The powder XRD and in-situ XRD experiments were performed using Bruker D8 Discover X-ray diffractometer with a nonmonochromated Cu Kα X-ray source. For in-situ XRD measurements, the positive electrode was covered by a titanium foil with a small hole which was covered with tape. The signals were received by the planar detector in a still mode during the testing process. The positive electrodes were fresh, and each pattern took 90 s to acquire at 1.5C charge and 0.75C discharge. TGA was performed on an STA-449C thermobalance in Ar atmosphere with a temperature ramp of 10 °C min^{-1}. Inductively coupled plasma-optical emission spectroscopy (ICP-OES) test was performed on a PerkinElmer Optima 4300DV spectrometer.

2.3. Electrochemical measurements

The cathode electrode paste film was prepared by mixing active materials, ketjen black, and polyvinylidene fluoride (7:2:1). Then, the paste film was dried for at least 12 h at 70 °C and pressed onto the Ti mesh. The mass loading of the active material was 7–9 mg cm^{-2}. The electrochemical measurements of the individual electrode sample were carried out in three-electrode setup (paste film on Ti mesh as the working electrode, SCE as reference electrode and Pt plate as counter-electrode) in 0.6 M K_2SO_4 electrolytes using an electrochemical workstation (CHI 760E/605E). Galvanostatic charge/discharge tests at high-rates were performed using a Battery Testing System (CT-ZWJ-4′S-T-1U) from Neware Technology Co.,Ltd., Shenzhen, China. The electrochemical impedance spectroscopy (EIS) was evaluated by using an electrochemical workstation (CHI 760E).

3. Results and discussion

3.1. Structural characterization

Ni_2Zn_1HCF, $Ni_{1.5}Zn_{1.5}HCF$, and Ni_1Zn_2HCF nanoparticles were synthesized through a simple coprecipitation method. The as-prepared Ni_2Zn_1HCF shows uniform nanoparticles with around 32.1 nm in diameter (Fig. 1a, e, Table S1). Energy-dispersive X-ray spectroscopy (EDS) mapping demonstrates the uniformed distribution of Zn, Ni, Fe, N, C, O and K elements in Ni_2Zn_1HCF (Fig. S1). $Ni_{1.5}Zn_{1.5}HCF$ also presents irregular shape (Fig. 1b), the particles stick together (Fig. S2a), and the elements distribute uniformly (Figs. S2b–i). The Ni_1Zn_2HCF sample shows some cubic morphologies (Fig. 1c), larger particle size up to 100 nm (Fig. S3a), and the elements also distribute uniformly (Figs. S3b–i). The elemental ratios of the as-prepared Ni_xZn_yHCF ($x + y = 3$, $x = 1$, 1.5
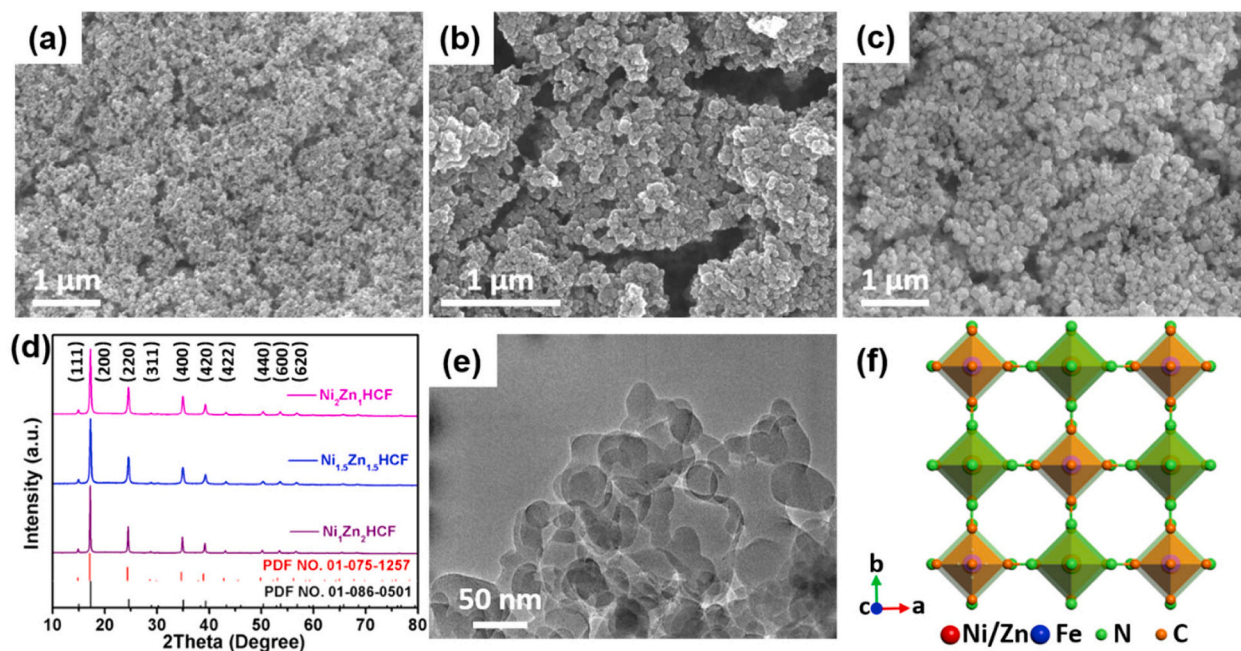
Fig. 1. Structural characterizations. SEM images of (a) Ni_2Zn_1HCF, (b) $Ni_{1.5}Zn_{1.5}HCF$, and (c) Ni_1Zn_2HCF powders. (d) XRD patterns (black: $Ni(Fe(CN)_6)_{0.667}\bullet(H_2O)_{3.333}$; red: $(Zn_3(Fe(CN)_6)_2)_{1.3333}\bullet(H_2O)_{19.22}$). (e) TEM image of Ni_2Zn_1HCF. (f) The as-synthesized powders have a cubic lattice.

or 2) powders were measured by inductively coupled plasma mass spectrometry (ICP-MS, Table S2), and the water content was determined through thermogravimetric analysis (TGA, Fig. S4). All the synthesized powders are well assigned to the $Ni(Fe(CN)_6)_{0.667}\bullet(H_2O)_{3.333}$ (JCPDS No. 01-086-0501) and $(Zn_3(Fe(CN)_6)_2)_{1.3333}\bullet(H_2O)_{19.22}$ (JCPDS No. 01-075-1257), both of which have a cubic lattice with *F-43 m* and *Fm-3m* space group, respectively, and no impurity is observed (Fig. 1d). For Ni_1Zn_2HCF with the highest content of Zn, the main diffraction peak, which represents (200) plane, shifts to low angle because Zn^{2+} has a larger radius than Ni^{2+} (Fig. S5) [34,35]. These three samples show a typical open framework structure of PBAs, in which linear rigid coordinated Fe–C≡N-M (M = Zn, Ni) linkages form the cubic framework with large hosting sites for potassium-ions (Fig. 1f) [36]. As for Ni_2Zn_1HCF, the cell parameters were determined as a = b = c = 10.250675 Å and $\alpha = \beta = \gamma = 90°$ *via* Rietveld refinement analysis [37]. Ni_0Zn_3HCF and Ni_3Zn_0HCF samples with cubic phase were also

synthesized (Fig. S6). Calculated from nitrogen adsorption-desorption isotherm, the specific surface area is 249, 371 and 428 $m^2\ g^{-1}$ for the as-prepared Ni_2Zn_1HCF, $Ni_{1.5}Zn_{1.5}HCF$ and Ni_1Zn_2HCF, respectively (Figs. S7a,b,c). The pore-size distribution curves indicate that the pore diameter for Ni_2Zn_1HCF, $Ni_{1.5}Zn_{1.5}HCF$ and Ni_1Zn_2HCF is centered at 40, 70 and 70 nm, respectively (Figs. S7d,e,f), which is mainly piled-pores.

X-ray photoelectron spectroscopy (XPS) measurements were conducted to determine the chemical states of the elements in the as-prepared powders (Fig. S8). The peaks at approximately 708.4 eV and 721.5 eV are originated from $Fe^{II}2p_{3/2}$ and $Fe^{II}2p_{1/2}$ in $[Fe^{II}(CN)_6]^{4-}$ and those at 709.9 eV and 723.5 eV are assigned to $Fe^{III}2p_{3/2}$ and $Fe^{III}2p_{1/2}$ in $[Fe^{III}(CN)_6]^{3-}$ (Fig. 2a) [38]. It is found that the Fe in Ni_0Zn_3HCF is mainly in +2 state while those in the other four samples are mainly in +3 state, which is probably due to the unstable Ni_0Zn_3HCF. N 1s spectra of Ni_3Zn_0HCF, Ni_1Zn_2HCF, $Ni_{1.5}Zn_{1.5}HCF$ and Ni_2Zn_1HCF show
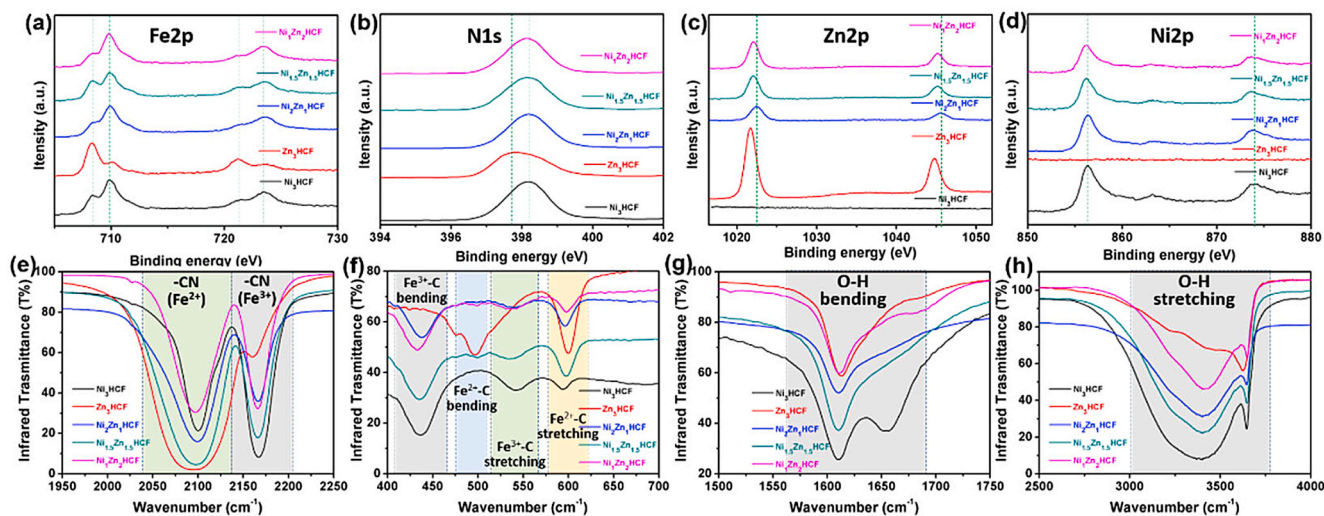
Fig. 2. Characterizations of chemical states and properties. XPS spectra of (a) Fe 2p, (b) N 1s, (c) Zn 2p, and (d) Ni 2p of the pristine materials. (e–h) FTIR spectra: (e) CN stretching region, (f) FeC bending/stretching region, (g) OH bending region, and (h) OH stretching region of the pristine materials.

symmetric peaks at around 398.2 eV, while the peak of Ni_0Zn_3HCF situated at around 397.9 eV is asymmetric (Fig. 2b). The binding energy of Zn 2p derived from Ni_0Zn_3HCF shows 0.2, 0.2 and 0.3 eV lower than those derived from Ni_1Zn_2HCF, $Ni_{1.5}Zn_{1.5}HCF$ and Ni_2Zn_1HCF, respectively (Fig. 2c). The lower binding energy values of N 1s and Zn 2p indicate the weakened connection of Zn–N coordinate bond in Ni_0Zn_3HCF than that in Ni_1Zn_2HCF, $Ni_{1.5}Zn_{1.5}HCF$ and Ni_2Zn_1HCF, which makes Zn easier to leach into solution [39,40]. Ni_3Zn_0HCF and Ni_2Zn_1HCF show little higher binding energy of Ni 2p than that in $Ni_{1.5}Zn_{1.5}HCF$ and Ni_1Zn_2HCF (Fig. 2d), indicating the decreased binding energy of Ni–N coordinate bond in the latter two samples, probably due to the higher content of the unstable Zn^{2+}. Fourier-transform infrared spectroscopy (FTIR) was also applied to characterize the

chemical properties of these five samples (Fig. S9). The peaks at around 2100 and 2170 cm^{-1} are assigned to $-CN(Fe^{2+})$ and $-CN(Fe^{3+})$ stretching, respectively (Fig. 2e) [41]. Compared to Ni_0Zn_3HCF, Ni_3Zn_0HCF show sharper peaks and higher wavenumbers, indicating the latter one is of better-defined structure [38]. The transmittance of $-CN$ (Fe^{3+}) stretching is much lower than that of $-CN(Fe^{2+})$ stretching in Ni_0Zn_3HCF sample, while in Ni_3Zn_0HCF sample, the transmittance of $-CN(Fe^{3+})$ stretching is higher than that of $-CN(Fe^{2+})$ stretching, also confirming that the Fe in Ni_0Zn_3HCF is mainly in +2 state. For Ni_1Zn_2HCF, $Ni_{1.5}Zn_{1.5}HCF$ and Ni_2Zn_1HCF samples, the transmittance of $-CN(Fe^{3+})$ stretching is little lower than that of $-CN(Fe^{2+})$ stretching. From 400 cm^{-1} to 700 cm^{-1}, C–Fe bonds characteristics are displayed in Fig. 2f. Ni_3Zn_0HCF sample shows a main peak at around 430 cm^{-1}
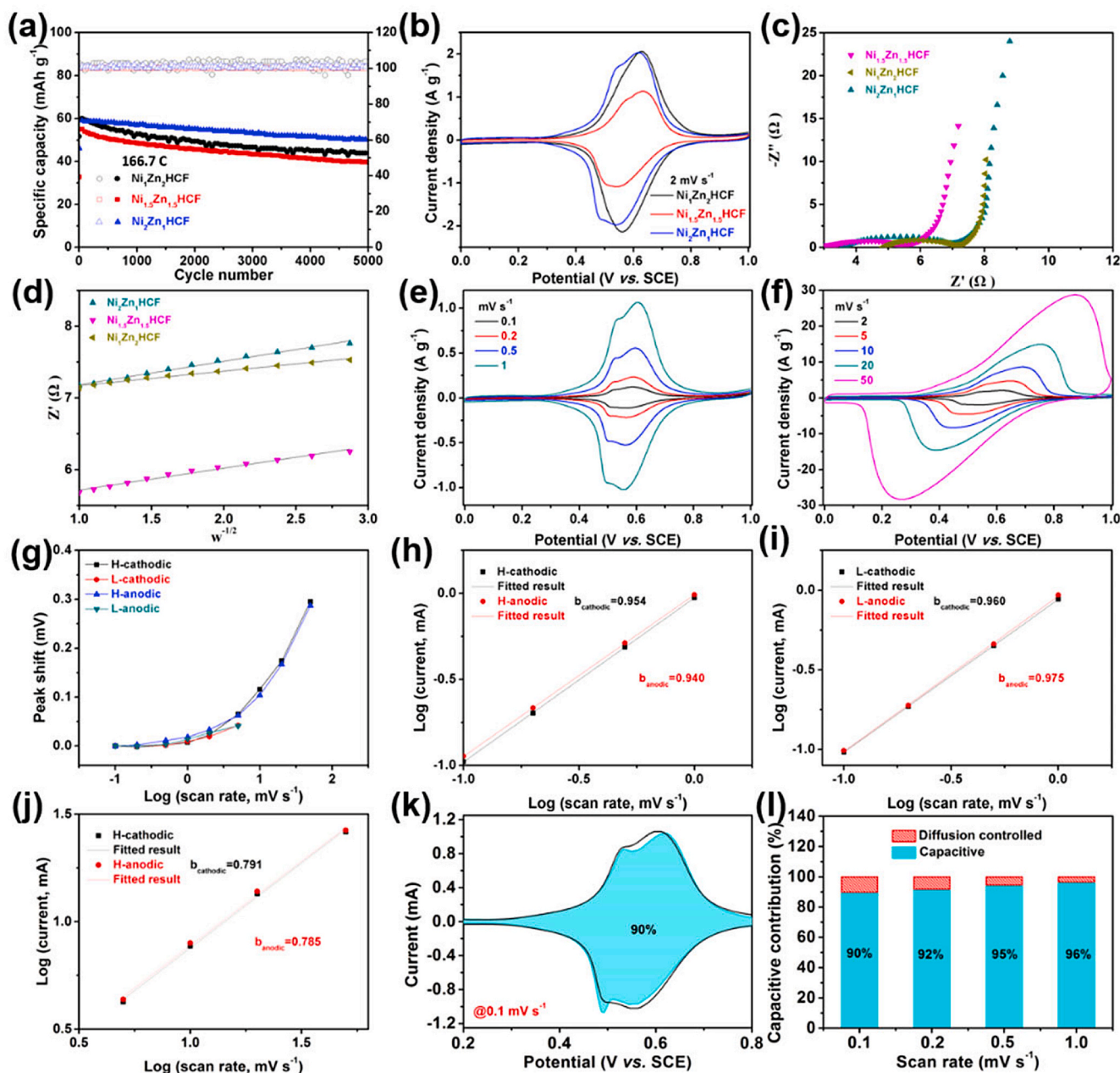
Fig. 3. Electrochemical characterizations. (a) Cycling performances at 166.7C and (b) CV curves at 2 mV s^{-1}. (c) Potentiostatic EIS spectra and (d) corresponding plots of the real part of impedance as a function of the inverse square root of angular frequency in the Warburg region. CV curves at (e) 0.1–1.0 mV s^{-1} and (f) 2–50 mV s^{-1}. (g) The variation of the cathodic/anodic peak voltage with the sweep rate. The relationship of the peak current (i_p) and the scan rate (mV s^{-1}): (h) high redox peaks and (i) low redox peaks between 0.1 and 1.0 mV s^{-1}; (j) high redox peaks between 5 and 50 mV s^{-1}. (k) Capacitive contribution (sky blue part) and diffusion contribution (void part) at 0.1 mV s^{-1}. (l) Normalized capacitive (water blue part) and diffusion-controlled (rosy part) contribution ratios from 0.1 to 1.0 mV s^{-1}.

assigned to Fe^{3+}-C bending, a lower peak at around 540 cm^{-1} assigned to Fe^{3+}-C stretching, and a small peak at around 580 cm^{-1} assigned to Fe^{2+}-C stretching, and no peak is found at Fe^{2+}-C bending area [42]. As for Ni_0Zn_3HCF sample, no obvious peak is observed at Fe^{3+}-C stretching and bending area, while a broad peak at 490 cm^{-1} with shoulders of Fe^{2+}-C bending and a sharp peak at 600 cm^{-1} Fe^{2+}-C stretching are well defined, indicating that Fe is mainly in +2 state. For the other three samples, the spectra shape resembles that of Ni_3Zn_0HCF sample, except the stronger Fe^{2+}-C stretching peak. The broader peaks of transmittance of O–H bending and stretching Ni_3Zn_0HCF sample than the other samples are observed (Fig. 2g, h). Based on the above analysis, the valence state of Fe in Ni_0Zn_3HCF is mainly +2 while that in the rest four sample is mainly +3 probably because of the instability of Ni_0Zn_3HCF [43]. Therefore, the replace of Zn^{2+} with Ni^{2+} can realize the high structural stability in Ni_xZn_yHCF by reducing the content of the unstable Zn–N coordinate bond.

3.2. Electrochemical characterization

The electrochemical characteristics were investigated *via* a three-electrode setup with a saturated calomel electrode (SCE) and a platinum plate as the reference electrode and counter electrode, respectively. In the long-term cycling test at the current density of 166.7C (1C = 60 mA g^{-1}), the second discharge capacity of Ni_3Zn_0HCF electrode is 39.4 mAh g^{-1}, and 38.3 mAh g^{-1} is maintained after 3000 cycles, corresponding to a capacity retention of 97.2% (Fig. S10a). The Ni_0Zn_3HCF electrode shows a severe capacity decay of 76.7% after only 300 cycles, which is highly related to the unstable Ni_0Zn_3HCF in aqueous K_2SO_4 solution [18,36]. Although Ni_3Zn_0HCF exhibits much higher cycling stability than Ni_0Zn_3HCF, the redox potential (0.43/0.51 V *vs.* SCE) of the former one shows lower than that of the latter one (0.68/0.83 V *vs.* SCE) by 285 mV (Fig. S10b). Thus, the electrochemical properties of Ni_xZn_yHCF type electrode materials are supposed to be compromised in terms of cyclability and redox potential, in which, synergistically, Ni^{2+} enhances the stability and Zn^{2+} lifts the redox potential. The second discharge capacities of Ni_1Zn_2HCF, $Ni_{1.5}Zn_{1.5}HCF$ and Ni_2Zn_1HCF electrodes are 60.0, 55.8, and 58.7 mAh g^{-1}, respectively (Fig. 3a). After cycling for 5000 times, 73.2% (43.9 mAh g^{-1}), 71.1% (39.7 mAh g^{-1}), and 85.5% (50.2 mAh g^{-1}) capacity retention are achieved for Ni_1Zn_2HCF, $Ni_{1.5}Zn_{1.5}HCF$ and Ni_2Zn_1HCF electrodes, respectively. The Ni_xZn_yHCF type electrode materials truly show much better cyclability than Ni_0Zn_3HCF electrode materials while it is not competitive with Ni_3Zn_0HCF electrode materials. In the cyclic voltammetry (CV) test (Fig. 3b), it is in consistence with our supposition that the average equilibrium potentials (all at around 0.6 V *vs.* SCE) of these three electrodes are in the medium of those of the Ni_3Zn_0HCF and Ni_0Zn_3HCF electrode materials. In addition, Ni_1Zn_2HCF electrode shows the highest redox potential and the lowest polarization, while the $Ni_{1.5}Zn_{1.5}HCF$ electrode exhibits the largest polarization and the smallest capacity, which is consistent with the cycling performance. Among these three type Ni_xZn_yHCF electrode materials, Ni_2Zn_1HCF exhibits the best cyclability and considerable equilibrium potential due to the synergistic effect between Ni^{2+} and Zn^{2+}.

On the basis of Electrochemical impedance spectroscopy (EIS) analysis (Fig. 3c), the charge transfer impedance (R_{ct}) values of Ni_1Zn_2HCF, $Ni_{1.5}Zn_{1.5}HCF$ and Ni_2Zn_1HCF electrodes are 2.2 Ω, 2.65 Ω and 3.4 Ω, respectively. The corresponding fitting values of the slope of Z′ *vs.* $\omega^{-1/2}$ plots (ω is the angular frequency) are 0.202, 0.305 and 0.327, respectively (Fig. 3d). It can be seen that Ni_2Zn_1HCF electrode has moderate R_{ct} and ionic diffusion coefficient among them. At 0.1 mV s^{-1}, the CV curve of Ni_2Zn_1HCF electrode shows two redox peaks of 0.512/0.527 V and 0.563/0.586 V, corresponding to a low polarization of 7.5 mV and 11.5 mV, respectively (Fig. 3e). When the scan rate increases to 1.0 mV s^{-1}, two pairs of redox peaks of 0.503/0.541 V and 0.556/0.604 V, corresponding to a polarization of 19 mV and 24 mV, respectively, are observed, revealing the fast ionic diffusion kinetics

[44]. At the scan rates larger than 2.0 mV s^{-1}, the redox peaks at lower potential (L-cathodic/-anodic) submerge in the left shoulder of the redox peaks at higher potential (H-cathodic/-anodic) because of the increased polarization (Fig. 3f). The polarization of the H-cathodic/anodic peaks rapidly increases to 302.5 mV (0.268/0.873 V) and the shift of the cathodic/anodic peaks voltage with the scan rate shows a region of small peak shift followed by increased shift at 2.0 mV s^{-1} (Fig. 3g). It is assumed that the relationship of the current and scan rate obeys the power-law leading to equation (1):

$$i = av^b \tag{1}$$

where a and b can be adjusted [45]. When the b-value is 0.5, the electrochemical processes are diffusion-controlled, and a b-value of 1.0 indicates that the electrochemical processes are surface-controlled. For the scan rate in the arrangement of 0.1–1.0 mV s^{-1}, the b-value of the H-cathodic, H-anodic, L-cathodic, L-anodic peaks is 0.954, 0.940, 0.960 and 0.975, respectively (Fig. 3h,i). At scan rates over 2.0 mV s^{-1}, the b-value for the H-cathodic and H-anodic peaks is decreased to 0.791 and 0.785, respectively (Fig. 3j). To determine the capacitive and diffusion-controlled contribution ratio from 0.1 to 1 mV s^{-1}, the equations of $i = k_1v$ (capacitive) $+ k_2v^{1/2}$ (diffusion-controlled) and $i/v^{1/2} = k_1v^{1/2} + k_2$ are utilized [46]. At 0.1 mV s^{-1}, the capacitive contribution accountes for 90% of the total capacity (Fig. 3k). When the scan rates increase from 0.2 to 1.0 mV s^{-1}, that value increases from 92% to 96% (Fig. 3l). Thus, it can be illustrated that the electrochemical kinetics at low rates (<2.0 mV s^{-1}) are nearly surface-controlled, i.e. near-pseudocapacitive, and the electrochemical kinetics is suppressed at high-rates (>2.0 mV s^{-1}) for the increased the ohmic contribution [45, 47]. The $Ni_{1.5}Zn_{1.5}HCF$ and Ni_1Zn_2HCF also show near-pseudocapacitive intercalation mechanism (Fig. S11).

In the long-term cycling test at the rate of 333C, the second discharge capacity of Ni_2Zn_1HCF electrode is 48.9 mAh g^{-1}. After cycling for 10,000 cycles, 90.4% of the capacity is retained, and the coulombic efficiency is around 99% (Fig. S12). At a higher rate of 500C, the second discharge capacity is 48.4 mAh g^{-1}, of which 89.6% can be remained after cycling for 30,000 times, with coulombic efficiency of around 100%, indicating the extremely high cycling stability of Ni_2Zn_1HCF electrode (Fig. 4a). In the rate range from 5C to 10C, 20C, 30C, 50C, 100C, 200C, 300C, 500C, 800C, and 1000C, the average discharge capacity reaches 66.0 mAh g^{-1}, 63.9 mAh g^{-1}, 62.8 mAh g^{-1}, 62.2 mAh g^{-1}, 61.6 mAh g^{-1}, 60.9 mAh g^{-1}, 60.3 mAh g^{-1}, 60.0 mAh g^{-1}, 58.9 mAh g^{-1}, 53.1 mAh g^{-1}, and 43.8 mAh g^{-1}, respectively (Fig. 4b). From 5C to extremely high-rate of 1000C, 66% capacity retention is achieved and Fig. 4c displays the corresponding charge/discharge profiles. Based on the active materials and the discharge curves, the highest specific power density is up to 13.2 kW kg^{-1}. After cycling under extremely high-rate of 1000C and returning the rate to 5C (average discharge capacity of 62.9 mAh g^{-1}), a capacity recovery of 95.3% is obtained, revealing the extremely high-rate capability of the Ni_2Zn_1HCF electrode materials. The excellent rate performance can be ascribed to the high specific surface area and fast near-pseudocapacitive intercalation mechanism. During the initial eight discharge cycles, the coulombic efficiency slowly increases from 87.8% to 97.8%, probably due to the irreversible ionic extraction. At the rates >5C, the coulombic efficiency is as high as 99%. During the subsequent 80,000 times long-life span cycling at 1000C, the electrode exhibits a negligible capacity decay of 0.000385% per cycle, also indicating the Ni_2Zn_1HCF electrode materials have extremely high-rate capability and strong cycling stability. In comparison with other reported electrode materials for aqueous batteries, the Ni_2Zn_1HCF electrode shows much superiority in rate capability and cyclability (Table 1).

To investigate the electrochemical storage mechanism and structural evolution processes, *in-situ* cell was constructed with Ni_2Zn_1HCF as the cathode, Zn plate as the anode and 0.6 M K_2SO_4 as the electrolyte. During the charging processes of Ni_2Zn_1HCF electrode at 1.5C, (220)
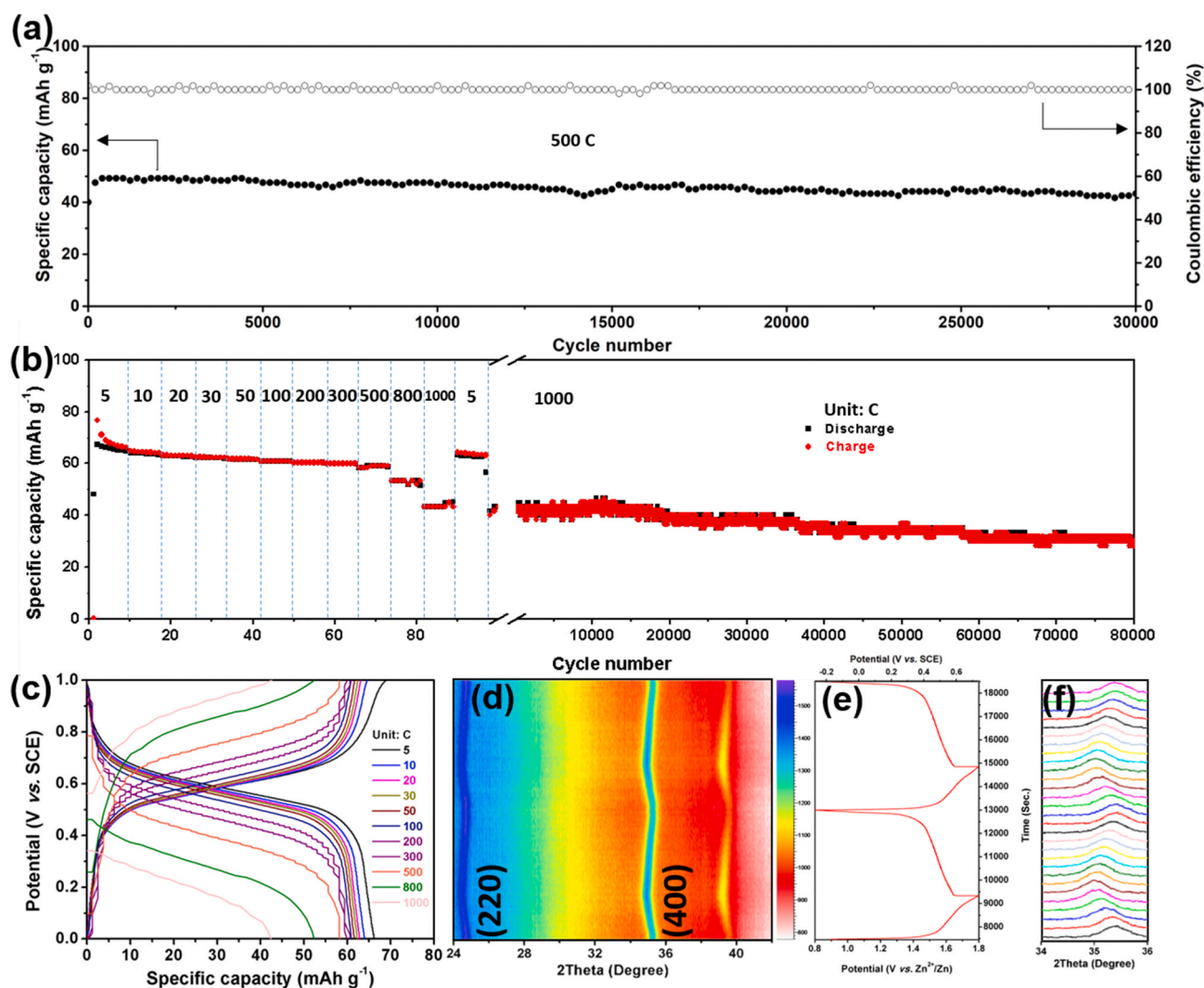
Fig. 4. Investigations of long-term cyclability and storage mechanism of Ni$_2$Zn$_1$HCF in 0.6 M K$_2$SO$_4$ electrolytes. (a) Cycling performance at 500C. (b) Rate performance of Ni$_2$Zn$_1$HCF at rate ranging from 5 to 1000C and subsequent cycling performances at 1000C, and (c) the corresponding charge/discharge profiles. *In-situ* XRD characterizations of Ni$_2$Zn$_1$HCF with Zn plate as anode at 1.5C charge and 0.75C discharge: (d) *In-situ* 2 D XRD patterns, (e) corresponding charge/discharge profiles and (f) 1 D XRD patterns.

and (400) diffraction peaks shift slightly to low angles, indicating the small increment of the lattice parameters due to the oxidation of [Fe^{II}(CN)$_6$]$^{4-}$ groups to [Fe^{III}(CN)$_6$]$^{3-}$ and K$^+$ extraction (Fig. 4d,e) [17, 49]. Upon the discharge processes at 0.75C, these two main diffraction peaks shift back to the original positions with the reduction of [Fe^{III}(CN)$_6$]$^{3-}$ groups to [Fe^{II}(CN)$_6$]$^{4-}$ and K$^+$ intercalation. Because of the radius of [Fe^{II}(CN)$_6$]$^{4-}$ groups is larger than that of [Fe^{III}(CN)$_6$]$^{3-}$ groups, the structural evolution of Ni$_2$Zn$_1$HCF is contributed to both the K$^+$ intercalation/extraction and [Fe^{III}(CN)$_6$]$^{3-}$/[Fe^{II}(CN)$_6$]$^{4-}$ groups interconversion. After two integrate cycles, the main diffraction peaks exhibit continuous and reversible shifting, illustrating the high reversibility of the solid-solution K$^+$ intercalation/extraction and [Fe^{III}(CN)$_6$]$^{3-}$/[Fe^{II}(CN)$_6$]$^{4-}$ groups interconversion in Ni$_2$Zn$_1$HCF [50, 51]. The well reversible shifting of the corresponding 1 D diffraction peak of the (400) crystalline plane is also displayed and no new peak forms (Fig. 4f). Above *in-situ* XRD results reveal that the K$^+$ storage mechanism of Ni$_x$Zn$_y$HCF cathode is solid-solution intercalation/extraction reaction.

4. Conclusion

Near-pseudocapacitive and super-stable bimetallic Ni$_x$Zn$_y$HCF (x +

y = 3, x = 1, 1.5, or 2) serial Prussian blue analogues cathode materials are developed and well-studied for extremely high-rate and long-term cycling life aqueous PIBs. As a representative, Ni$_2$Zn$_1$HCF cathode shows an extraordinary high-rate capability of 1000C with a capacity retention of 66% compared to the capacity at 5C rate and a high capacity recovery of 95.3% when return to 5C due to the large sufeace area and fast near-pseudocapacitive intercalation mechanism. It exhibits a high-stable cyclability of 30,000 times at 500C with a capacity retention of 90%. A negligible capacity decay of 0.000385% per cycle is shown at 1000C for 80,000 times cycling, which further proves this cathode promising for ultra-fast and high-stable aqueous PIBs. *Via* electrochemical and structural analysis, a synergistic effect between stable Ni^{2+} and high-voltage Zn^{2+} in Ni$_2$Zn$_1$HCF is demonstrated. In addition, the near-pseudocapacitive intercalation/extraction behavior of the Ni$_2$Zn$_1$HCF cathode is revealed, as the fitted *b*-value of multiple sweep CV is > 0.94 at scan rates lower than 2.0 mV s^{-1}. *In-situ* XRD illustrates the highly reversible solid-solution K$^+$ intercalation/extraction mechanism in Ni$_2$Zn$_1$HCF cathode. These research results show a promising route to building ultrafast and long-service aqueous PIBs for grid-scale energy storage and intermittent power supply.

Table 1

The electrode performance comparison of our work and other aqueous batteries reported previously. The specific capacity is based on the active cathode materials.

Cathode material	Rate capability	Discharge capacity	Cyclability	Ref.
CuHCF	67% retention ($83C = 4.98$ A g^{-1})	59.14 mAh g^{-1} ($0.83C = 50$ mA g^{-1})	40,000 cycles, 83% retention	Ref. [48]
KNiFeHCF	54.4% retention ($500C = 40$ A g^{-1})	77.4 mAh g^{-1} ($5C = 400$ mA g^{-1})	5000 cycles, 95.6% retention	Ref. [30]
KFeMnHCF	65.4% retention ($120C = 15.6$ A g^{-1})	130 mAh g^{-1} ($10C = 1.3$ A g^{-1})	10,000 cycles, 70% retention	Ref. [27]
KFeHCF	24% retention ($60C = 9$ A g^{-1})	160 mAh g^{-1} ($0.5C = 75$ mA g^{-1})	1000 cycles, 94.3% retention	Ref. [20]
ZnHCF	60% retention ($300C = 25.8$ A g^{-1})	78.7 mAh g^{-1} ($2C = 172$ mA g^{-1})	100 cycles, 86.4% retention	Ref. [31]
Ni_2Zn_1HCF	66% retention ($1000C = 60$ A g^{-1})	66 mAh g^{-1} ($5C = 300$ mA g^{-1})	30,000 cycles, 90% retention	This work

Declaration of competing interest

The authors declare that they have no known competing financial interests or personal relationships that could have appeared to influence the work reported in this paper.

CRediT authorship contribution statement

Meng Huang: Conceptualization, Investigation, Writing - original draft, Resources, Writing - review & editing, Supervision. **Xuanpeng Wang:** Investigation, Writing - original draft, Resources, Writing - review & editing, Conceptualization, Supervision. **Jiashen Meng:** Resources, Writing - review & editing, Conceptualization, Supervision. **Xiong Liu:** Conceptualization, Resources, Writing - review & editing. **Xuhui Yao:** Conceptualization, Resources, Writing - review & editing. **Ziang Liu:** Conceptualization, Resources, Writing - review & editing. **Liqiang Mai:** Conceptualization, Investigation, Supervision.

Appendix A. Supplementary data

Supplementary data to this article can be found online at https://doi.org/10.1016/j.nanoen.2020.105069.

References

[1] K.M. Muttaqi, M.R. Islam, D. Sutanto, Future power distribution grids: integration of renewable energy, energy storage, electric vehicles, superconductor, and magnetic bus, IEEE Trans. Appl. Supercond. (29) (2019) 1–5.

[2] P. Denholm, T. Mai, Timescales of energy storage needed for reducing renewable energy curtailment, Renew. Energy 130 (2019) 388–399.

[3] F. Keck, M. Lenzen, A. Vassallo, M. Li, The impact of battery energy storage for renewable energy power grids in Australia, Energy 173 (2019) 647–657.

[4] O. Krishan, S. Suhag, An updated review of energy storage systems: classification and applications in distributed generation power systems incorporating renewable energy resources, Int. J. Energy Res. 43 (2019) 6171–6210.

[5] B.R. Sutherland, Charging up stationary energy storage, Joule (3) (2019) 1–3.

[6] A.R. Dehghani-Sanij, E. Tharumalingam, M.B. Dusseault, R. Fraser, Study of energy storage systems and environmental challenges of batteries, Renew. Sustain. Energy Rev. 104 (2019) 192–208.

[7] C. Curry, Lithium-ion battery costs and market, Bloomberg New Energy Finance (5) (2017).

[8] H. Kim, J. Hong, K.Y. Park, H. Kim, S.W. Kim, K. Kang, Aqueous rechargeable Li and Na ion batteries, Chem. Rev. 114 (2014) 11788–11827.

[9] N. Yabuuchi, K. Kubota, M. Dahbi, S. Komaba, Research development on sodium-ion batteries, Chem. Rev. 114 (2014) 11636–11682.

[10] D. Kundu, E. Talaie, V. Duffort, L.F. Nazar, The emerging chemistry of sodium ion batteries for electrochemical energy storage, Angew. Chem. Int. Ed. 54 (2015) 3431–3448.

[11] Y. Li, C. Yang, F. Zheng, Q. Pan, Y. Liu, G. Wang, T. Liu, J. Hu, M. Liu, Design of TiO_2@C hierarchical tubular heterostructures for high performance potassium ion batteries, Nano Energy 59 (2019) 582–590.

[12] N. Alias, A.A. Mohamad, Advances of aqueous rechargeable lithium-ion battery: a review, J. Power Sources (274) (2015) 237–251.

[13] J.O.G. Posada, A.J. Rennie, S.P. Villar, V.L. Martins, J. Marinaccio, A. Barnes, C. F. Glover, D.A. Worsley, P.J. Hall, Aqueous batteries as grid scale energy storage solutions, Renew. Sustain. Energy Rev. 68 (2017) 1174–1182.

[14] M. Huang, M. Li, C. Niu, Q. Li, L. Mai, Recent advances in rational electrode designs for high-performance alkaline rechargeable batteries, Adv. Funct. Mater. 29 (2019), 1807847.

[15] W. Li, J.R. Dahn, D.S. Wainwright, Rechargeable lithium batteries with aqueous electrolytes, Science 264 (1994) 1115–1118.

[16] D. Bin, F. Wang, A.G. Tamirat, L. Suo, Y. Wang, C. Wang, Y. Xia, Progress in aqueous rechargeable sodium-ion batteries, Adv. Energy Mater. (8) (2018), 1703008.

[17] C.D. Wessells, S.V. Peddada, R.A. Huggins, Y. Cui, Nickel hexacyanoferrate nanoparticle electrodes for aqueous sodium and potassium-ion batteries, Nano Lett. 11 (2011) 5421–5425.

[18] L. Zhang, L. Chen, X. Zhou, Z. Liu, Towards high-voltage aqueous metal-ion batteries beyond 1.5 V: the zinc/zinc hexacyanoferrate system, Adv. Energy Mater. (5) (2015), 1400930.

[19] K. Lu, B. Song, J. Zhang, H. Ma, A rechargeable Na-Zn hybrid aqueous battery fabricated with nickel hexacyanoferrate and nanostructured zinc, J. Power Sources 321 (2016) 257–263.

[20] C. Liu, X. Wang, W. Deng, C. Li, J. Chen, M. Xue, R. Li, F. Pan, Engineering fast ion conduction and selective cation channels for a high-rate and high-voltage hybrid aqueous battery, Angew. Chem. Int. Ed. 57 (2018) 7046–7050.

[21] P. Jiang, H. Shao, L. Chen, J. Feng, Z. Liu, Ion-selective copper hexacyanoferrate with an open-framework structure enables high-voltage aqueous mixed-ion batteries, J. Mater. Chem. (5) (2017) 16740–16747.

[22] Y. Wang, J. Yi, Y. Xia, Recent progress in aqueous lithium-ion batteries, Adv. Energy Mater. (2) (2012) 830–840.

[23] L. Suo, O. Borodin, T. Gao, M. Olguin, J. Ho, X. Fan, C. Luo, C. Wang, K. Xu, "Water-in-salt" electrolyte, Science 350 (2015) 938–943.

[24] L. Suo, O. Borodin, W. Sun, X. Fan, C. Yang, F. Wang, T. Gao, Z. Ma, M. Schroeder, A. von Cresce, S.M. Russell, M. Armand, A. Angell, K. Xu, C. Wang, Advanced high-voltage aqueous lithium-ion battery enabled by "Water-in-bisalt" electrolyte, Angew. Chem. Int. Ed. 55 (2016) 7136–7141.

[25] Y. Yamada, K. Usui, K. Sodeyama, S. Ko, Y. Tateyama, A. Yamada, Hydrate-melt electrolytes for high-energy-density aqueous batteries, Nat. Energy (1) (2016) 1–9.

[26] D. Bin, Y. Wen, Y. Wang, Y. Xia, The development in aqueous lithium-ion batteries, J. Energy Chem. 27 (2018) 1521–1535.

[27] L. Jiang, Y. Lu, C. Zhao, L. Liu, J. Zhang, Q. Zhang, X. Shen, J. Zhao, X. Yu, H. Li, X. Huang, L. Chen, Y.-S. Hu, Building aqueous K-ion batteries for energy storage, Nat. Energy 4 (2019) 495–503.

[28] L. Chen, H. Shao, X. Zhou, G. Liu, J. Jiang, Z. Liu, Water-mediated cation intercalation of open-framework indium hexacyanoferrate with high voltage and fast kinetics, Nat. Commun. 7 (2016), 11982.

[29] D. Su, A. McDonagh, S.Z. Qiao, G. Wang, High-capacity aqueous potassium-ion batteries for large-scale energy storage, Adv. Mater. 29 (2017), 1604007.

[30] W. Ren, X. Chen, C. Zhao, Ultrafast aqueous potassium-ion batteries cathode for stable intermittent grid-scale energy storage, Adv. Energy Mater. (8) (2018), 1801413.

[31] M. Huang, J. Meng, Z. Huang, X. Wang, L. Mai, Ultrafast and cation insertion-selected zinc hexacyanoferrate for 1.9 V K-Zn hybrid aqueous battery, J. Mater. Chem. (8) (2020) 6631–6637.

[32] V. Augustyn, P. Simon, B. Dunn, Pseudocapacitive oxide materials for high-rate electrochemical energy storage, Energy Environ. Sci. (7) (2014) 1597–1614.

[33] X. Dong, L. Chen, J. Liu, S. Haller, Y. Wang, Y. Xia, Environmentally-friendly aqueous Li (or Na)-ion battery with fast electrode kinetics and super-long life, Sci. Adv. (2) (2016), e1501038.

[34] Y. Zhao, P. Zhang, Microstructure and microwave dielectric properties of low loss materials $Li_3(Mg_{0.95}A_{0.05})_2NbO_6$ (A = Ca^{2+}, Ni^{2+}, Zn^{2+}, Mn^{2+}) with rock-salt structure, J. Alloys Compd. 658 (2016) 744–748.

[35] M. Pasta, R.Y. Wang, R. Ruffo, R. Qiao, H.-W. Lee, B. Shyam, M. Guo, Y. Wang, L. A. Wray, W. Yang, M.F. Toney, Y. Cui, Manganese-cobalt hexacyanoferrate cathodes for sodium-ion batteries, J. Mater. Chem. (4) (2016) 4211–4223.

[36] J.-G. Wang, Z. Zhang, X. Zhang, X. Yin, X. Li, X. Liu, F. Kang, B. Wei, Cation exchange formation of Prussian blue analogue submicroboxes for high-performance Na-ion hybrid supercapacitors, Nano Energy 39 (2017) 647–653.

[37] R. Oishi-Tomiyasu, M. Yonemura, T. Morishima, A. Hoshikawa, S. Torii, T. Ishigaki, T. Kamiyama, Application of matrix decomposition algorithms for singular matrices to the Pawley method in Z-Rietveld, J. Appl. Crystallogr. 45 (2012) 299–308.

[38] L. Shen, Z. Wang, L. Chen, Prussian blues as a cathode material for lithium ion batteries, Chem. Eur J. (20) (2014) 12559–12562.

[39] Q. Yang, F. Mo, Z. Liu, L. Ma, X. Li, D. Fang, S. Chen, S. Zhang, C. Zhi, Activating C-coordinated iron of iron hexacyanoferrate for Zn hybrid-ion batteries with 10,000-cycle lifespan and superior rate capability, Adv. Mater. 31 (2019), 1901521.

[40] J. Liu, X. Li, A.I. Rykov, Q. Fan, W. Xu, W. Cong, C. Jin, H. Tang, K. Zhu, A. S. Ganeshraja, R. Ge, X. Wang, J. Wang, Zinc-modulated Fe-Co Prussian blue analogues with well-controlled morphologies for the efficient sorption of cesium, J. Mater. Chem. (5) (2017) 3284–3292.

[41] R. Martinez-Garcia, M. Knobel, E. Reguera, Thermal-induced changes in molecular magnets based on Prussian blue analogues, J. Phys. Chem. B 110 (2006) 7296–7303.

[42] C.W. Ng, J. Ding, L.M. Gan, Structure and magnetic properties of Zn-Fe cyanide, J. Phys. D Appl. Phys. 34 (2001) 1188.

[43] P. Gravereau, E. Garnier, Structure de la Phase Cubique de I'Hexacyanoferrate(III) de Zinc: $Zn_3[Fe(CN)_6]_2 \bullet nH_2O$, Acta Crystallogr. C (40) (1984) 1306.

[44] F. Cheng, H. Wang, Z. Zhu, Y. Wang, T. Zhang, Z. Tao, J. Chen, Porous $LiMn_2O_4$ nanorods with durable high-rate capability for rechargeable Li-ion batteries, Energy Environ. Sci. (4) (2011) 3668–3675.

[45] V. Augustyn, J. Come, M.A. Lowe, J.W. Kim, P.L. Taberna, S.H. Tolbert, H. D. Abruna, P. Simon, B. Dunn, High-rate electrochemical energy storage through Li$^+$ intercalation pseudocapacitance, Nat. Mater. 12 (2013) 518–522.

[46] X. Hu, X. Sun, S.J. Yoo, B. Evanko, F. Fan, S. Cai, C. Zheng, W. Hu, G.D. Stucky, Nitrogen-rich hierarchically porous carbon as a high-rate anode material with ultra-stable cyclability and high capacity for capacitive sodium-ion batteries, Nano Energy 56 (2019) 828–839.

[47] D.S. Charles, M. Feygenson, K. Page, J. Neuefeind, W. Xu, X. Teng, Structural water engaged disordered vanadium oxide nanosheets for high capacity aqueous potassium-ion storage, Nat. Commun. 8 (2017) 15520.

[48] C.D. Wessells, R.A. Huggins, Y. Cui, Copper hexacyanoferrate battery electrodes with long cycle life and high power, Nat. Commun. (2) (2011) 2550.

[49] A. Dostal, G. Kauschka, S.J. Reddy, F. Scholz, Lattice contractions and expansions accompanying the electrochemical conversions of Prussian blue and the reversible and irreversible insertion of rubidium and thallium ions, J. Electroanal. Chem. (406) (1996) 155–163.

[50] X. Wang, X. Xu, C. Niu, J. Meng, M. Huang, X. Liu, Z. Liu, L. Mai, Earth abundant Fe/Mn-based layered oxide interconnected nanowires for advanced K-ion full batteries, Nano Lett. 17 (2017) 544–550.

[51] W. Ren, M. Qin, Z. Zhu, M. Yan, Q. Li, L. Zhang, D. Liu, L. Mai, Activation of sodium storage sites in Prussian blue analogues *via* surface etching, Nano Lett. 17 (2017) 4713–4718.

Jiashen Meng received his B.S. degree from Wuhan University of Technology in 2015 and he is currently working toward his Ph.D. degree in Materials Science at Wuhan University of Technology. From 2018 to 2019, he was a visiting Ph.D. student at Massachusetts Institute of Technology. His current research focuses on developing new nanomaterials and chemistry for energy conversion and storage devices.

Xiong Liu received his B.S. degree from Wuhan University of Technology in 2016. He is currently working toward the Ph.D. degree and his research interests focus on the controllable structure design for energy storage/conversion and reconstruction chemistry in electrocatalysis.

Xuhui Yao is a Ph.D. student at Advanced Technology Institute, University of Surrey, working with Dr. Yunlong Zhao and Prof. Ravi Silva. His research focuses on electrode materials for sodium/potassium-ion batteries, all-solid-state lithium battery and in-situ characterisation.

Meng Huang received his B.S. degree from Wuhan University of Technology in 2016. He is currently working toward the Ph. D. degree and his research interests focus on the materials for aqueous electrolyte based energy storage and the ionic storage mechanisms.

Ziang Liu received his B.Sc. degree from Wuhan University of Technology in 2017. He is currently a Ph.D. candidate under the supervision of Prof. Liqiang Mai in State Key Laboratory of Advanced Technology for Materials Synthesis and Processing. He is working on the electrospinning fabricating one-dimensional nanostructure for high energy-density battery.

Xuanpeng Wang received his Ph.D. degree from Wuhan University of Technology in 2019. Now, he is an assistant professor of Physics at Wuhan University of Technology. His current research focuses on physical&chemical in potassium-ion batteries, sodium-ion batteries, high temperature molten salt batteries, and sustainable recycling technology for secondary batteries.

Liqiang Mai is Chair Professor of Materials Science and Engineering at Wuhan University of Technology (WUT). He is the winner of the National Natural Science Fund for Distinguished Young Scholars and Fellow of the Royal Society of Chemistry. He received his PhD from WUT in 2004 and carried out his postdoctoral research at Georgia Institute of Technology in 2006–2007. He worked as an advanced research scholar at Harvard University in 2008–2011 and at University of California, Berkeley in 2017. His current research interests focus on new nanomaterials for electrochemical energy storage and micro/nano energy devices.